A photoplethysmographic imaging system with supplementary capabilities

Francisco CORRAL[*], Gonzalo PAEZ, Marija STROJNIK

Centro de Investigaciones en Óptica A.C., Apartado Postal 1-948, C.P. 37000,
León, Guanajuato, México

[*]Corresponding author: lfcorral@cio.mx

We perform a temporal and spectral analysis of simulated and experimental photoplethysmographic signals. We obtain technical requirements for an advanced photoplethysmographic imaging system able to add photoplethysmographic waveform and oximetry maps to the conventional measurements. The imaging system is centered on measuring the pulsatile signals produced by diffuse reflectance on the inner layers of the skin. We consider controlled illumination conditions for the system, with visible and near infrared components. This work comprises backscattering evaluation, waveform analysis and spectral dependence of photoplethysmographic signal. We determine the resolution requirement for the system by evaluating the amplitude of the backscattered signal using Monte Carlo simulations. We determine the bandwidth limit for the signal acquisition by Fourier analysis from a set of plethysmographic waveforms. Finally, the spectral dependence of the system is obtained from experimental results. We establish the requirements for the photoplethysmographic imaging system, including the source, subject and detector conditions.

Keywords: photoplethysmographic (PPG) imaging, remote PPG, remote oximetry, diffuse reflectance spectroscopy.

1. Introduction

Monitoring vital signs in patients, including oxygen content in blood and tissues, is essential when human life is threatened, or when medical procedures intended to preserve or enhance it are performed. For the last three decades, pulse oximetry has been routinely used in anesthesiology and intensive-care units for assessing pulse rate and blood oxygen saturation in patients. The acquisition of pulse oximetry signals is performed using finger or ear probes [1]. Even though it is a non-invasive technique, conditions in patients such as wounds or burned skin prevent the use of contact probes. In these cases, remote signal acquisition is the best alternative.

Several efforts for obtaining remote monitoring of vital signs, including pulse oximetry, have been reported in literature. The most recent advances in these technol-

ogies comprise photoplethysmographic (PPG) imaging with high spatial resolution [2], remote oximetry using diffuse correlation spectroscopy [3], patented systems for mapping blood perfusion during surgery [4], and diffuse optical imaging using spatial modulated illumination sources [5]. Moreover, there are new methods for obtaining high contrast imaging of blood vessels [6]. There are also robust algorithms for patients in high motion situations [7]. Peripheral blood circulation assessment has been achieved by monitoring the amplitude and phase of blood pulsation [8]. Autoregressive modeling has been used to improve results of PPG imaging outside of controlled illumination environments [9]. Mobile device cameras have now the potential for monitoring heart rate and blood oxygen saturation [10]. PPG has been combined with complementary techniques to improve its capabilities. One of them is a laser speckle contrast analysis, which increases the capability of the system for assessing skin blood supply [11]. Another technique is infrared thermography imaging, this technique supplements heart and respiratory rates and skin perfusion with temperature behavior [12]. The latter systems represent significant advances in the remote monitoring of vital signs.

The results exposed in this manuscript demonstrate the capability of PPG imaging for obtaining PPG waveform and oximetry maps, which are supplementary parameters to those already reported.

2. Remote PPG and pulse oximetry

PPG is the optical method for measuring volumetric changes in organs. We use it for evaluating blood volume changes in tissue due to the rhythmic impulsion of blood into the vascular system, caused by diastolic and systolic phases of the cardiac cycle [13]. A PPG system in the most basic form requires a light source and a photodetector. These two elements are properly arranged to produce a suitable PPG signal. An oximetry system integrates at least two PPG systems in different wavelengths (usually red and infrared bands) to derive blood oxygen saturation (SpO_2) measurements.

Under normal conditions, the principal components of the red blood cells are oxygenated hemoglobin (oxyhemoglobin, HbO2) and deoxygenated hemoglobin (deoxyhemoglobin, Hb). The blood oxygen saturation is defined as the ratio of oxyhemoglobin content to total hemoglobin content, $SpO_2 = HbO_2/(HbO_2 + Hb)$. PPG systems are designed to obtain heart rates and blood oxygen saturation values. They also provide information about general hemodynamic status, hydration status, cardiac arrhythmias, blood pressure and stiffness of the cardiovascular system [14].

It is possible to obtain maps of tissue oxygenation using several sources and detectors [15]. Recent studies explore the remote (contactless) extraction of PPG signals. The need for contact with the patient to obtain heart and respiratory rates has been eliminated [16]. Emerging problems as motion artifacts have been reduced with robust algorithms [17]. Finally, there exist guidelines for migrating remote measurements from point to area regions [18]. Several of the latter experimental setups are oriented to pulse oximetry techniques. Multispectral PPG imaging signals have been obtained *in vivo* with promising results for oximetry [19]. The same method has obtained pulse

oxigrams for *in vitro* samples [20]. Another experimental setup has shown alternative results but has also presented technological limitations [21].

Concentration of substances in fluids is generally detected using Beer–Lambert law. Blood is a fluid carrying several components, and oximetry is focused on detecting its HbO_2 concentration. New improved expressions have been developed for oximetry computation but commercial oximeters use empirical look up tables [22, 23]. The first step to perform pulse oximetry measurements is obtaining a clear PPG signal. Next, the amplitude of the pulsatile component is divided by the amplitude of its corresponding steady component to obtain a spectral ratio. Finally, spectral ratios are then divided (usually red ratio/infrared ratio) to obtain the ratio of ratios (RoR),

$$RoR = \frac{\Delta I_R / I_R}{\Delta I_{IR} / I_{IR}} \tag{1}$$

where ΔI is the pulsatile component and I is the steady component, subscripts R and IR stand for red and infrared, respectively. The look up table is a tabular function that relates the computed ratio of ratios with the actual SpO_2 value. It fits the simplified form of the theoretic calibration curve given by the following equation:

$$SpO_2 = \frac{k_1 - k_2 RoR}{k_3 - k_4 RoR} \tag{2}$$

where k_1–k_4 are the coefficients of empirical calibration. Extinction coefficients of Hb and HbO_2, and spectral response of source and sensitivity detector are implicit in these coefficients.

A camera-based instrument (CBI) is a measuring system with a camera acting as its basic component. The shortest integration time of the camera defines its maximum frame rate. The minimum change of radiant power that can be detected defines its sensitivity. The maximum amount of radiation that can be detected without saturation and the sensitivity define its dynamic range. In this work we also present a study on the required frame rate and dynamic range of a CBI for monitoring bidimensional arrays of PPG signals. We may be able to obtain waveforms and oxygen saturation maps from the measured PPG signals.

The analysis presented in the next sections confirms the potential of the PPG imaging system for becoming the next patient monitoring and treatment bedside system. In the next section, we determine the spectral change in diffuse reflected light by the skin due to the change in the HbO_2 and Hb concentration. We perform Monte Carlo simulations in order to demonstrate this phenomenon.

3. Materials and methods

The skin is the largest organ of the human body. It is a soft tissue made up of multiple layers that cover and protect the body from external agents. The outermost layer of the skin is the epidermis, the dermis is below it and the innermost layer is the hypo-

dermis. *Plexus superficialis* and *plexus profundus* are the vessel beds that supply blood to dermis. We have a special interest in the modulation of light produced by them. The first step in our analysis is the Monte Carlo simulation of light propagation through human skin. The purpose of the simulation is to determine the fraction and the spectral composition of the light reflected from the skin layers.

3.1. Backscattering analysis

We perform simulations using Monte Carlo modeling of photon transport in multilayered tissues [24]. The algorithm uses the Henyey–Greenstein phase function to determine the scattering direction of light in multilayered turbid media. We use a five-layer tissue model [25]. The incident light is a monochromatic and infinitesimally thin beam perpendicular to tissue. We use four wavelengths for the simulations: 577, 633, 805 and 940 nm. Optical parameters for the five-layer model are well-documented for 577 and 633 nm, but not for 805 and 940 nm. However, an established IR source for commercial pulse oximeters is 940 nm [23]. Three-wavelength techniques use the isosbestic point of HbO_2 and Hb, 805 nm [26]. We calculate optical parameters for the five-layer model of skin for 805 and 940 nm from blood, epidermis and dermis parameters reported

T a b l e 1. Optical parameters of skin used in simulations. Parameters are for diastolic phase and oxygen saturation $SpO_2 = 100\%$.

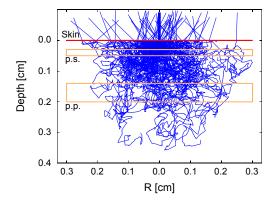| Skin layer	λ [nm]	μ_a [cm^{-1}]	μ_s [cm^{-1}]	g	N	d [μm]
Epidermis	577	10.70	120.0	0.78	1.5	100
	633	4.30	107.0	0.79		
	805	1.66	18.3	0.80		
	940	0.64	16.2	0.80		
Dermis	577	3.00	205.0	0.78	1.4	200
	633	2.70	187.0	0.82		
	805	1.18	11.4	0.80		
	940	0.77	9.7	0.80		
Dermis with *plexus superficialis*	577	5.20	219.0	0.78	1.4	200
	633	3.30	192.0	0.82		
	805	1.41	40.1	0.81		
	940	1.18	33.0	0.81		
Dermis	577	3.00	205.0	0.78	1.4	900
	633	2.70	187.0	0.82		
	805	1.18	11.4	0.80		
	940	0.77	9.7	0.80		
Dermis with *plexus profundus*	577	6.00	225.0	0.78	1.4	600
	633	3.40	194.0	0.82		
	805	1.45	45.9	0.81		
	940	1.26	37.7	0.81		

Fig. 1. Monte Carlo simulation setup. The incident photon packets reach the skin and interact with the inner layers. Several photon packets reach *plexus superficialis* (p.s.) and *plexus profundus* (p.p.) (highlighted), return to the surface and exit the skin carrying PPG information.

in [27–29]. Table 1 shows the optical parameters used for simulations when oxygen saturation $SpO_2 = 100\%$ and the cardiac cycle exhibits the diastolic phase.

We run simulation algorithm 48 times, one time for each combination of parameters (oxygen saturation–wavelength–phase). Six oxygen saturation values are used: 50, 70, 80, 90, 95 and 100%, and four wavelengths are used: 577, 633, 805 and 940 nm. Two phases of the cardiac cycle are simulated: diastole and systole.

The optical parameters for dermis with *plexus superficialis* and dermis with *plexus profundus* are linear combinations of absorption and scattering coefficients for the respective concentration of HbO_2 and Hb. The systolic phase optical parameters are modified according to the increment of blood volume into the *plexus* layers. Figure 1 illustrates the simulation process. The central beam is the source of illumination. The highlighted layers represent dermis with *plexus superficialis* and dermis with *plexus profundus*. We use 10^6 photon packets for every simulation. Several photon packets reach the inner layers and return to the surface carrying information about the blood status. Blood volume variation into the layers, due to a cardiac cycle, modifies the number of reflected photon packets. Spectral absorption variation in blood, due to SpO_2 changes, also modifies this reflection.

3.2. Waveform analysis

We perform Fourier analysis to the waveform results obtained by ALLEN and MURRAY [30]. In this experiment they recorded PPG pulse waveforms from ears, fingers and toes of 116 subjects. The subject ages ranged from 13 to 72 years and they were classified in four age groups: younger than 30 years, 30–39 years, 40–49 years and 50 years of age or older. They found that the PPG waveform from an individual changes its characteristics along the years because of the ageing of the cardiovascular system. Figure 2 exhibits the set of waveforms classified by age groups, each shape
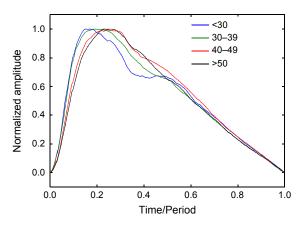
Fig. 2. Set of waveforms classified by age groups. Waveforms are amplitude and time normalized. We observe from this graph that waveforms become smoother with age.

plot is formed from the average of at least 20 subjects. Period and amplitude of the signals have been normalized to 1. We observe smooth variations in the waveform of the older group, while variations in the waveform of the younger group are rougher.

We may represent each waveform from this set as a harmonic signal using Fourier series. Morphological differences between the signals can be distinguished comparing their Fourier series coefficients up to a defined *n*-th harmonic. The extraction of the Fourier series coefficients from a discrete signal is defined by the following equation:

$$c_n = \frac{1}{N} \sum_{k=0}^{N-1} f(k) \exp\left(-\frac{2\pi i n k}{N}\right) \tag{3}$$

where N represents the number of samples in the period, k is the sample index, and n is the number of harmonic, being $n = 1$ the fundamental frequency, the heart rate (HR). The waveform reconstruction is obtained by the following equation:

$$f(k) = \sum_{n=-m}^{m} c_n \exp\left(\frac{2\pi i n k}{N}\right) \tag{4}$$

where m is the maximum number of harmonics defined for the signal reconstruction.

3.3. Spectral analysis

The last analysis of this work is performed for selecting the optimal wavelength range for remote oximetry. In a previous work from our group we showed a method for multispectral analysis of remote PPG signals [31]. In that work we obtained backscattered signals from human forehead for wavelengths from 380 to 980 nm. The source of illumination that we used presented a broadband continuous spectrum. We measured the remote PPG signal in 380–980 nm band using a spectrometer with 0.762 nm of resolution. Raw data from readings contained a mix of PPG signal (wanted) as well as

noise (unwanted). A commercial pulse co-oximeter served as reference for HR and HR variability determination. Frequency-domain components of amplitude of raw signal at every wavelength were obtained by means of the Fourier transform. Amplitude of PPG signal was determined by direct integration of the known HR band. Amplitude of noise was determined as the maximum amplitude in any other band of the same width. We computed the direct SNR between the PPG signal and the maximum noise.

Finally we determined that the optimal wavelengths for PPG signal extraction by diffuse reflection are the bands from 480 to 610 nm and from 800 to 925 nm. Moreover, we intend to use wavelengths that allow the discrimination between Hb and HbO_2 [32]. The absorption chart for these blood components shows the bands in which each component is the dominant absorber. Figure 3 shows three curves, the first is the SNR obtained for remote PPG. The second is the ratio of the molar extinction coefficients for Hb over HbO_2, $\varepsilon_{Hb}/\varepsilon_{HbO2}$. The third curve shows the ratio $\varepsilon_{HbO2}/\varepsilon_{Hb}$. Data for ε_{Hb} and ε_{HbO2} are obtained from [33].
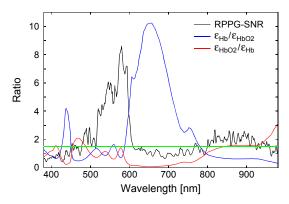

Fig. 3. Curves for SNR for remote PPG, the absorption coefficients ratio Hb over HbO_2 and its reciprocal HbO_2 over Hb. The threshold of 1.5 is helpful for deciding the optimal bands for remote oximetry.

We define a threshold to ensure the effects of one absorber are at least 50% larger than the effects of the other. The suitable regions for reliable remote PPG intended for oximetry computations are the intersections of the curves in which PPG signal and blood component relative absorption ratios are over the indicated threshold.

In the next sections we show the obtained results and establish the minimum technical requirements for the PPG imaging system.

4. Results

4.1. Backscattering analysis

The light reflected by the skin shows a compound reflection pattern which is dependent on the bidirectional reflectivity distribution function (BRDF) [34], and also on the distance to the center of the incident beam. Figure 4 shows the BRDF as a function of angle
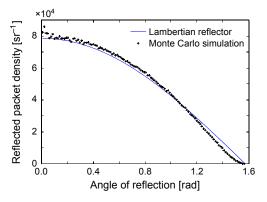
Fig. 4. BRDF as a function of angle of reflection. Skin behaves as an almost Lambertian reflector.
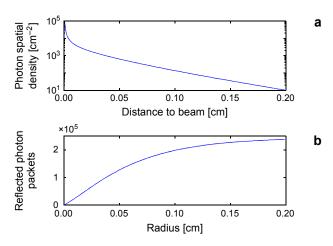

Fig. 5. Results of Monte Carlo simulation. Photon spatial density of reflected light (**a**). Normalized number of photon packets reflected *vs.* circle of radius *R* (**b**). The number of photon packets reflected shows a reduction as long as the distance from beam center increases.

of reflection. The Monte Carlo simulation results for SpO_2 = 100%, λ = 633 nm and diastole phase, show that 241696 photon packets are reflected (24.17%). The angular distribution obtained from simulation is superimposed to the curve of a Lambertian reflector. For comparison purposes, this Lambertian reflector reflects the same number of photon packets.

Figure 5 depicts the reflection distribution as a function of distance between the center of the incident beam and the exit point of its corresponding backscattered part. This figure also shows the number of photon packets that are reflected inside the circle of radius *R* (centered on the entry point). The reflection reduces its photon density as long as the reflection point increases its distance with the entry point of the beam. The emitted fraction by the circle of radius *R* around the incident beam is 80% for *R* = 0.1 cm, 97% for *R* = 0.2 cm and 99.6% for *R* = 0.3 cm.

T a b l e 2. Average number of reflected photon packets. We average the diastolic and systolic phases of the cardiac cycle.

SpO$_2$ [%]	Wavelength [nm]			
	577	633	805	940
50	189204	237599	133205	151159
70	187970	238760	133063	149500
80	187227	239754	133243	148615
90	186549	240319	133119	147655
95	185968	240645	133166	147303
100	186095	241071	133214	146960

We simulate one million of incident photon packets and retrieve the number of reflected packets. We use the 48 combinations of oxygen saturation–wavelength–phase described before. After simulating the diastolic and systolic phases of the cardiac cycle for every wavelength and SpO$_2$ value, we obtain the respective #dia and #sys number of reflected photon packets. Table 2 shows the average number of reflected photon packets between the diastolic and systolic phases (#dia + #sys)/2. This average number is called the steady-state (DC) part of the PPG signal.

Table 2 shows that the average number of packets reflected for 577 and 940 nm wavelengths decreases when the blood oxygen saturation increases. The reflection for 805 nm light does not exhibit any trend. The reflection for 633 nm increases when the blood oxygen saturation does.

Table 3 shows the difference between the number of reflected photon packets for the diastolic and systolic phases. We consider this difference the pulsatile (AC) part of the PPG signal.

T a b l e 3. Difference between reflected packets for diastolic and systolic phase.

SpO$_2$ [%]	Wavelength [nm]			
	577	633	805	940
50	17073	3273	−15229	−14965
70	17531	2514	−15324	−14054
80	16710	2440	−15515	−13562
90	16964	1847	−15434	−13063
95	16644	2070	−15299	−13024
100	16840	1250	−15299	−12925

We observe from Table 3 that the weakest pulsatile signal corresponds to the wavelength of 633 nm. The rest of the wavelengths show higher amplitudes. We note that 805 and 940 nm signals exhibit the maximum number of reflected photon packets during the systolic phase, while 577 and 633 nm signals exhibit its corresponding maximum during the diastolic phase.
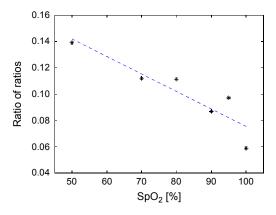
Fig. 6. Ratio of ratios computation from Monte Carlo simulations, and its respective linear fit. Tendency for ratio of ratios is downwards *vs*. oxygen saturation.

The suitable wavelengths for oxygen saturation computation are 633 and 940 nm. The goal for our computation is to achieve SpO_2 results with resolution of 1%. We perform a minimum square linear fit of the AC signal with respect to SpO_2. From this fit we obtain the change of photon packets corresponding to the desired resolution. A change of 1% in oxygen saturation corresponds to a variation of 35 photon packets for 633 nm, and 42 packets for 940 nm. The dynamic range of detectors is defined as the ratio of the largest non-saturating input signal to the smallest detectable input signal. In this case, our maximum expected signal is 241696 photon packets (633 nm, SpO_2 = 100%, diastole), while the minimum expected change is 35 photon packets (633 nm, ΔSpO_2 = 1%). The minimum dynamic range for a useful detector is 6906:1 or 77 dB.

Figure 6 shows a downward trend in the ratio of ratios from simulation results with respect to the increasing of SpO_2. We fit this set of points to an invertible function in order to obtain the oximetry calibration function. If a look up table is necessary, we can construct it from the calibration function.

4.2. Waveform analysis

We determined the Fourier series coefficients for every waveform. After that, we obtained a set of reconstructions for each waveform using 2, 3 and up to 8 harmonics. The Pearson correlation coefficient (PCC) is a measure of the strength of linear dependence between two variables [35]. We finally compare every set of reconstructions with the original waveform by means of the PCC. Figure 7 shows the relationship between the amount of harmonics used to reconstruct each waveform and the PCC associated to its original waveform.

We illustrate the amount of harmonics required to reconstruct the waveform with a linear dependence given for the PCC, $r = 0.999$. To reach this value, we need 5 harmonics for the elder group but 6 for the younger one. Given a reconstruction using
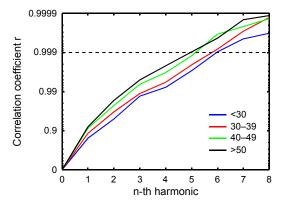
Fig. 7. Number of harmonics used to reconstruct each waveform *vs.* the PCC associated to its original waveform. Smooth shapes need fewer coefficients than rough shapes to reach a high PCC.

6 harmonics for every age group, it is possible to discern between the reconstructed waveform and the rest of them.

4.3. Spectral analysis

From the analysis of Fig. 3 we found that Hb is the dominant absorber of blood in 425–450 nm and 590–780 nm bands. HbO_2 is the dominant absorber of blood in 455–490 nm and 850–980 nm bands. Discarding wavelengths with poor remote PPG signal extraction (below the threshold), we conclude that the best band for remote detection of Hb volume changes is 590–610 nm. In the same way we found that HbO_2 volume changes can be best detected in 850–910 nm band. The spectral response of CCD and CMOS cameras is optimal for the implementation of the proposed PPG imaging system with oximetry capability.

5. Conclusions

The setup for the proposed PPG imaging system is described next. The illumination source will project the beam perpendicular to the skin of the subject. The subject under test should remain immobile, so the noise remains as low as possible. The camera will be in front of the subject. The angle between the source and the camera would vary but is recommended to remain low to maximize the amount of light captured.

There are slight differences between the BDRF of Monte Carlo simulation of skin and the Lambertian reflector (Fig. 4). This result shows that the skin behaves as an almost Lambertian reflector and allows a high degree of freedom in the camera location of the experimental setup.

Uniform illumination over the skin may be described as an infinite set of infinitesimally thin beams. Each one of these beams will produce the reflection pattern shown in Fig. 5. The reflected light will be uniform due to the superposition of the individual

reflections of the beams. This uniform reflected light is suitable for obtaining PPG and oximetry maps from skin regions.

Monte Carlo simulation demonstrated that the infrared (940 nm) pulsatile signal is five to ten times greater than the red (633 nm) signal. The simulation also showed that any of these signals is tens to hundreds of times greater than its respective variation in pulsatile amplitude due to a SpO_2 change of 1%. To achieve the precision of commercial pulse oximeters, a high dynamic range camera (DR > 6906:1) must be used.

The ratio of ratios obtained from Monte Carlo simulation for the selected wavelengths shows a downward trend (Fig. 6). A monotonically decreasing calibration function should be constructed for relating the ratio of ratios with the respective oxygen saturation level.

The basal heart rate for an adult is 60 to 80 beats per minute (bpm), while for intense activity it can reach 200 or more bpm. We demonstrated previously the need for a reconstruction up to the 6th harmonic to identify a waveform. Considering the Nyquist sampling theorem, the minimum frame rate for acquiring PPG imaging signal able to contain not only a heart rate but also morphological information at 200 bpm is 40 frames per second (fps). The morphological information contained in the PPG imaging signal will be helpful for determining homogeneous blood irrigation. With this feature the system will be able to identify abnormal tissue, arterial occlusion and poor perfusion regions.

In order to develop the advanced PPG imaging system with remote oximetry features, we will employ a source of illumination with a continuous spectrum covering the band from 590 to 910 nm, as a minimum requirement. We propose a quartz tungsten halogen lamp with color temperature t_c > 3000 K for the source.

A visible–near infrared camera is suitable to cover the required spectral band. The wavelength selection will be performed by bandpass interference filters. Despite the fact of the reduced Hb detection band (590–610 nm), it is precisely around 600 nm where these cameras have their highest quantum efficiency. The increased spectral irradiance of the source for the infrared region and the wider HbO_2 detection band (850–910 nm) compensate the reduced quantum efficiency of the camera in such region. The dynamic range of the camera must be greater than 6909:1 and the frame rate has to be more than 40 fps.

The CBI will be able to monitor extended regions in subjects, unlike the single spots of contact probes. The increased frame rate of the system will allow reconstruction of PPG waveforms. The spectral features will provide pulse oximetry capabilities to the system. The combination of all these features will produce a novel monitoring device, but the high-level camera that meets these requirements may be very expensive.

However, requirements were established considering extreme conditions (200 bpm, 6th harmonic reconstruction and SpO_2 = 1%). For a standard monitoring with a resting patient, the heart rate should be less than 100 bpm. Oximetry resolution of the system can be reduced to detect only significant SpO_2 differences (>5%). Finally, we may also reduce the bandwidth limit because 99% of the PPG waveform is concentrated in 4 or less harmonics. Taking into account the above considerations, it is feasible the reduc-

tion of the dynamic range of the camera to 1381:1 and the frame rate to 14 fps. Using a more affordable camera that meets these new requirements, we still would have an instrument able to detect abnormal tissue, arterial occlusion and poor perfusion regions.

With this work we demonstrated the feasibility of an advanced PPG imaging system. In addition, we set the basis for the improvement of the existing PPG monitoring systems.

References

[1] ALLEN J., *Photoplethysmography and its application in clinical physiological measurement*, Physiological Measurement **28**(3), 2007, pp. R1–R39.

[2] KAMSHILIN A.A., MIRIDONOV S., TEPLOV V., SAARENHEIMO R., NIPPOLAINEN E., *Photoplethysmographic imaging of high spatial resolution*, Biomedical Optics Express **2**(4), 2011, pp. 996–1006.

[3] TING LI, YU LIN, YU SHANG, LIAN HE, CHONG HUANG, SZABUNIO M., GUOQIANG YU, *Simultaneous measurement of deep tissue blood flow and oxygenation using noncontact diffuse correlation spectroscopy flow-oximeter*, Scientific Reports **3**, 2013, article 01358.

[4] SPIGULIS J., *Biophotonic technologies for non-invasive assessment of skin condition and blood microcirculation*, Latvian Journal of Physics and Technical Sciences **49**(5), 2012, pp. 63–80.

[5] O'SULLIVAN T.D., CERUSSI A.E., CUCCIA D.J., TROMBERG B.J., *Diffuse optical imaging using spatially and temporally modulated light*, Journal of Biomedical Optics **17**(7), 2012, article 071311.

[6] HSIN-YI TSAI, YI-JU CHEN, HAN-CHAO CHANG, KUO-CHENG HUANG, *Method to obtain the high contrast images of blood vessel for oxygen saturation calculation*, Proceedings of SPIE **8769**, 2013, article 87690F.

[7] DE HAAN G., JEANNE V., *Robust pulse rate from chrominance-based rPPG*, IEEE Transactions on Biomedical Engineering **60**(10), 2013, pp. 2878–2886.

[8] KAMSHILIN A.A., TEPOLOV V., NIPPOLAINEN E., MIRIDONOV S., GINIATULLIN R., *Variability of microcirculation detected by blood pulsation imaging*, PLoS ONE **8**(2), 2013, article e57117.

[9] TARASSENKO L., VILLARROEL M., GUAZZI A., JORGE J., CLIFTON D.A., PUGH C., *Non-contact video-based sing monitoring using ambient light and auto-regressive models*, Physiological Measurement **35**(5), 2014, pp. 807–831.

[10] KARLEN W., ANSERMINO J.M., DUMONT G.A., SCHEFFER C., *Detection of the optimal region of interest for camera oximetry*, Proceedings of the 35th Annual International Conference of the IEEE EMBS, July 3–7, 2013, Osaka, Japan, pp. 2263–2266.

[11] JAKOVELS D., RUBINS U., SPIGULIS J., *LASCA and PPG imaging for non-contact assessment of skin blood supply*, Proceedings of SPIE **8668**, 2013, article 866849.

[12] BLANIK N., ABBAS K.A., VENEMA B., BLAZEK V., LEONHARDT S., *Hybrid optical imaging technology for long-term remote monitoring of skin perfusion and temperature behavior*, Journal of Biomedical Optics **19**(1), 2014, article 016012.

[13] AOYAGI T., *Pulse oximetry: its invention, theory, and future*, Journal of Anesthesia **17**(4), 2003, pp. 259–266.

[14] SHELLEY K.H., *Photoplethysmography: beyond the calculation of arterial oxygen saturation and heart rate*, Anesthesia and Analgesia **105**(6), 2007, pp. S31–S36.

[15] HEBDEN J.C., SCHMIDT F.E.W., FRY M.E., SCHWEIGER M., HILLMAN E.M.C., DELPY D.T., ARRIDGE S., *Simultaneous reconstruction of absorption and scattering images by multichannel measurement of purely temporal data*, Optics Letters **24**(8), 1999, pp. 534–536.

[16] Verkruysse W., Svaasand L.O., Nelson J.S., *Remote plethysmographic imaging using ambient light*, Optics Express **16**(26), 2008, pp. 21434–21445.

[17] Cennini G., Arguel J., Aksit K., van Leest A., *Heart rate monitoring via remote photoplethysmography with motion artifacts reduction*, Optics Express **18**(5), 2010, pp. 4867–4875.

[18] Sijung Hu, Azorin-Peris V., Echiadis A., Jia Zheng, Ping Shi, *Development of effective photoplethysmographic measurement techniques: from contact to non-contact and from point to imaging*, Proceedings of the 31st Annual International Conference of the IEEE Engineering in Medicine and Biology Society, September 3–6, 2009, Minneapolis, U.S.A., pp. 6550–6553.

[19] Wieringa F.P., Mastik F., van der Steen A.F.W., *Contactless multiple wavelength photoplethysmographic imaging: a first step toward 'SpO$_2$ camera' technology*, Annals of Biomedical Engineering **33**(8), 2005, pp. 1034–1041.

[20] Wieringa F.P., Mastik F., Boks R.H., Visscher A., Bogers A. J.J.C., van der Steen A.F.W., *In vitro demonstration of an SpO$_2$-camera*, Computers in Cardiology **34**, 2007, pp. 749–751.

[21] Humphreys K., Ward T., Markham C., *Noncontact simultaneous dual wavelength photoplethysmography: a further step toward noncontact pulse oximetry*, Review of Scientific Instruments **78**(4), 2007, article 044304.

[22] Vazquez-Jaccaud C., Paez G., Strojnik M., *Noise-immune oximetry employing a new expression for oxygen saturation in blood*, Proceedings of SPIE **6678**, 2007, article 66781N.

[23] Webster J., *Design of Pulse Oximeters*, Institute of Physics, Bristol, 1997, pp. 21–55.

[24] Lihong Wang, Jacques S.L., Liqiong Zheng, *MCML – Monte Carlo modeling of light transport in multi-layered tissues*, Computer Methods and Programs in Biomedicine **47**(2), 1995, pp. 131–146.

[25] Tuchin V.V., *Tissue Optics: Light Scattering Methods and Instruments for Medical Diagnosis*, Second Edition, SPIE Press, Bellingham, 2007.

[26] Nitzan M., Engelberg S., *Three-wavelength technique for the measurement of oxygen saturation in arterial blood and in venous blood*, Journal of Biomedical Optics **14**(2), 2009, article 024046.

[27] Lister T., Wright P.A., Chappell P.H., *Optical properties of human skin*, Journal of Biomedical Optics **17**(9) 2012, article 090901.

[28] Roggan A., Friebel M., Dörschel K., Hahn A., Müller G., *Optical properties of circulating human blood in the wavelength range 400–2500 nm*, Journal of Biomedical Optics **4**(1), 1999, pp. 36–46.

[29] Salomatina E., Jiang B., Novak J., Yaroslavsky A.N., *Optical properties of normal and cancerous human skin in the visible and near-infrared spectral range*, Journal of Biomedical Optics **11**(6), 2006, article 064026.

[30] Allen J., Murray A., *Age-related changes in the characteristics of the photoplethysmographic pulse shapes at various body sites*, Physiological Measurement **24**(2), 2003, pp. 297–307.

[31] Corral L.F., Paez G., Strojnik M., *Optimal wavelength selection for noncontact reflection photoplethysmography*, Proceedings of SPIE **8011**, 2011, article 801191.

[32] Vazquez-Jaccaud C., Paez G., Strojnik M., *Wavelength selection method with standard deviation: application to pulse oximetry*, Annals of Biomedical Engineering **39**(7), 2011, pp. 1994–2009.

[33] Prahl S., *Tabulated molar extinction coefficient for hemoglobin in water*, http://omlc.ogi.edu/spectra/hemoglobin/summary.html, (access date: April 2014).

[34] Malacara D., Thompson B., *Handbook of Optical Engineering*, Marcel Dekker, New York, 2001, pp. 649–700.

[35] Krzanowski W., *Statistical Principles and Techniques in Scientific and Social Research*, Oxford University Press, New York, 2007.